RSC Advances

ROYAL SOCIETY OF CHEMISTRY

PAPER

View Article Online
View Journal | View Issue

Cite this: *RSC Adv.*, 2026, **16**, 6421

Synthesis and characterization of heterostructured carbon nanodots derived from *Pinus pinea* L. bark for enhanced Fe^{3+} sensing and antioxidant activity

Abidin Gümrükçüoğlu *

Pinus pinea L. bark residues were utilized for the environmentally friendly synthesis of PP300-3 carbon nanodots (synthesized *via* pyrolytic treatment at 300 °C for 3 hours). Comprehensive structural characterization employing high-resolution transmission electron microscopy (HR-TEM), scanning electron microscopy (SEM), X-ray diffraction (XRD), Fourier-transform infrared spectroscopy (FTIR), and X-ray photoelectron spectroscopy (XPS) revealed a hybrid nanostructure comprising crystalline graphitic domains and amorphous carbon regions. This heterogeneous structure provides excellent photoluminescent properties with a quantum yield of 3.8%. Photoluminescent characteristics were investigated through wavelength-dependent optical studies, revealing optimal photon emission efficiency at 320 nm. Screening experiments with thirty-three metal ions demonstrated that Fe^{3+} exhibited high selectivity. Although five metal ions (Au^{3+}, Bi^{3+}, Pd^{2+}, Pt^{2+}) caused some fluorescence quenching, only Fe^{3+} demonstrated a linear dose-dependent response suitable for quantitative analysis. With excellent analytical performance (R^2 = 0.9926, RSD < 2%, LOD = 35.43 μg L^{-1}), a simple spectrofluorometric protocol for Fe^{3+} determination was developed and validated in real water samples, achieving 99.56% recovery rates. Antioxidant evaluation using FRAP, CUPRAC, and DPPH assays demonstrated significant free-radical scavenging efficiency. Low SC_{50} concentrations (4.36 ± 0.92 mg mL^{-1}) indicate robust electron-transfer capacity and valuable antioxidant activity. In conclusion, PP300-3 carbon nanodots represent a versatile platform material with simple synthesis, environmentally friendly production, excellent analytical performance, and significant antioxidant activity, making them suitable for environmental monitoring, water quality control, and biomedical research.

Received 7th December 2025
Accepted 22nd January 2026

DOI: 10.1039/d5ra09455k

rsc.li/rsc-advances

1 Introduction

Carbon, one of the most abundant elements on Earth, serves as a fundamental building block of the biosphere and occupies a central position in nanomaterial research.[1,2] Continuous technological advancement has enabled new and functional materials to assume increasingly significant roles in modern life. Within this framework, carbon dots (CDs) have emerged as a compelling fluorescent nanomaterial class with promising applications across diverse fields including biological imaging, sensing, authentication technologies, and photocatalytic processes.[3–6] Since their initial characterization in 2004, fluorescent nanoparticles exhibiting favorable properties have been obtained from carbon nanotubes through electric discharge methods and gel electrophoresis techniques.[7]

Carbon dots are typically defined as carbon-based nanoparticles with diameters smaller than ten nanometers. The primary characteristics of these materials include size-dependent variable fluorescence emission, high photostability, and biological system compatibility.[8,9] These properties position them as ideal candidates for advanced imaging technologies. The resultant optical properties stem from quantum confinement effects and the presence of surface functional groups. Quantum confinement enables tunable fluorescence across a broad spectral range as particle dimensions vary,[4] while hydroxyl, amino, and carboxyl groups decorating the surface enhance carbon dot solubility and stability while facilitating facile surface modifications.[10]

In recent years, carbon dots have demonstrated substantial potential in overcoming limitations of conventional fluorescent probes in ultra-high resolution imaging. The principal drawbacks of classical fluorescent dyes—including diminished brightness, photobleaching susceptibility, and phototoxicity risks—substantially constrain their utility in advanced imaging techniques.[11,12] Carbon dots, conversely, offer distinct advantages including superior fluorescence quantum efficiency, photobleaching resistance, and excellent biocompatibility,[13] positioning them as increasingly preferred materials for ultra-resolution imaging applications compared to traditional dyes.

The attractiveness of these structures originates from exceptional physicochemical properties. These nanomaterials

Medicinal- Aromatic Plants Application and Research Centre, Artvin Coruh University, Artvin, 0800, Turkiye. E-mail: gumrukcuogluabidin@artvin.edu.tr

demonstrate good biocompatibility capability, robust physicochemical durability, pronounced aqueous dispersibility, and facile synthesis methodologies.[14–18] The utilization of industrial waste streams as precursor materials for carbon dot (CD) formulation provides significant advantages from both environmental sustainability and economic efficiency perspectives.[19,20] While optical and luminescence properties constitute the most prominent attributes, biological functionality has recently emerged as an intensive research focus.[21,22] Within this context, evaluation of free radical scavenging capacity represents a particularly relevant research direction.[23–27]

Synthetic protocols substantially determine the optical and fluorescence properties exhibited by these nanomaterials.[28] The mechanistic relationship between synthesis parameters and bioactive behavior remains incompletely characterized.[29] Bottom-up construction methodologies utilizing organic precursors facilitate rapid, cost-effective, and straightforward production pathways.[30] Industrial byproducts, agricultural waste streams, and municipal waste flows serve as applicable carbon precursors in bottom-up CD synthesis.[31,32] Consequently, these approaches integrate economic viability with environmental responsibility. Bottom-up strategies encompass diverse processing modalities including hydrothermal, solvothermal, chemical, electrochemical, microwave-assisted, and thermolytic protocols,[33] among which direct thermal decomposition demonstrates superior characteristics regarding cost-effectiveness, operational simplicity, and ecological compatibility.[34]

Fe^{3+} speciation analysis utilizing fluorescence spectroscopy constitutes a broadly investigated application domain.[35–37] While these methodologies provide high analytical sensitivity, their implementation demands extended synthesis and purification stages.[35–38] Certain studies employed synthetic reagents during synthesis and consequently lacked validation against authentic matrices.[39] Alternative approaches utilizing biogenic waste materials for CD preparation exist.[40–42] These similarly require prolonged conditioning protocols,[40,41] though selected investigations have remained restricted to cellular imaging applications.[41]

CD application for Sn^{2+} and Pd^{2+} determination has remained substantially limited, thereby necessitating development of optimized nanomaterial systems for these transition metal ions.[43–46] Gao and colleagues achieved subcellular Sn^{2+} localization utilizing confocal laser scanning microscopy.[43] However, the proposed CD synthesis protocol suffers from temporal demands and environmental incompatibility. Wu and associates employed waste eggshell membranes for CD production and investigated Sn^{2+}-induced fluorescence modulation.[44] Nevertheless, validation against authentic sample matrices was not performed. Pd^{2+} quantification has been insufficiently explored utilizing carbon-based nanostructures.[45,46] Sharma and colleagues confined their investigation to subcellular Pd^{2+} detection,[45] while Gao and collaborators extended applications to aqueous Pd^{2+} determination.[46] Despite these efforts, both studies incorporated synthetic reagents and extended synthesis procedures.

Thermal processing parameters exert decisive influence on resulting fluorescence properties.[47] CD samples derived from citric acid and ethylene derivatives were systematically examined regarding processing temperature and temporal parameters.[47] Subambient thermal conditions (*e.g.*, 150 °C) yielded excitation-independent emission spectra, whereas elevated temperatures (*e.g.*, 300 °C) produced excitation-dependent fluorescence quenching.[47] This investigation did not address metallic cations' regulatory effects on these spectroscopic phenomena.[47]

Thermal decomposition temperature substantially influences the morphological architecture of biomass-derived CD systems.[48,49] Sago processing waste yielded high-density fluorescent CDs with thermal temperature regulating carbonization progression.[48] Optimal emission intensity was achieved following 400 °C thermal processing. Cu^{2+} and Pb^{2+} determination was accomplished through fluorescence quenching mechanisms, demonstrating these materials' applicability.[48] Separately, Li and colleagues pyrolyzed meat processing waste at 220, 260, and 300 °C, obtaining nitrogen-containing fluorescent nanospheres.[49] Heating temperature substantially modulated particle dimensions, morphological configuration, and interfacial chemical functionalization.[49] Nevertheless, systematic investigation of thermal and temporal variables' effects on metal binding capabilities remains incomplete.

Within this context, the present investigation was designed to elucidate thermal decomposition conditions' effects on carbon nanodot (PP-CD) metal sensing capacity derived from *Pinus pinea* L. bark. Mediterranean pine bark underwent thermochemical processing under varied conditions, yielding PP-CDs. Fluorescence spectroscopy was employed to characterize interactions between synthesized PP-CDs and diverse metal species. PP-CD applicability for Fe^{3+} determination in authentic samples was demonstrated, and the prepared PP-CD structures exhibited pronounced free radical scavenging activity.

The present research was designed according to five fundamental objectives: (1) to develop an effective and environmentally benign pyrolysis synthesis protocol for high-functionality carbon nanodots from *Pinus pinea* bark—a renewable agricultural waste—thereby supporting circular economy principles and biomass valorization; (2) to comprehensively characterize the synthesized nanomaterials structural, morphological, compositional, and photoluminescent properties using complementary advanced analytical techniques (HR-TEM, SEM, XRD, FTIR, XPS) to establish structure–property relationships; (3) to investigate the synthesized carbon nanodots' photoluminescent characteristics and develop them as a novel fluorescence-based analytical platform for sensitive, selective, rapid, and quantitative determination of ferric (Fe^{3+}) ions in aqueous systems, alongside potential application in environmental water quality monitoring; (4) to systematically evaluate the nanomaterials' antioxidant and free radical scavenging capacity through multiple independent complementary assays (FRAP, CUPRAC, DPPH), thereby determining their potential in biomedical and therapeutic applications; and (5) to develop and validate a practical, rapid, economical, and user-friendly spectrofluorometric analytical procedure suitable for real-world

environmental applications, encompassing water quality surveillance, pollution monitoring, and biomedical research contexts.

2 Materials and methods

2.1 Instrumentation

A PTI QM-4 spectrofluorimeter equipped with a 1.0 nm slit width was utilized for fluorescence measurements in a 1 cm quartz cuvette. UV-Vis absorption spectra of PP-CNDs were recorded using an Analytik Jena Specord 21 spectrophotometer (Analytik Jena AG, Jena, Germany). The aqueous PP-CNDs solution was subjected to desiccation, and the resulting solid material was subsequently scraped to obtain a fine powder. This solid-state sample was subsequently subjected to X-ray photoelectron spectroscopy (XPS) and X-ray diffraction (XRD) analyses. For transmission electron microscopy (TEM) characterization, 1 mL of the aqueous CND solution was diluted with ethanol, deposited onto a carbon-coated copper grid, and air-dried at ambient temperature. Structural analysis was performed using a FEI TALOS F200S TEM instrument operating at 200 kV (Thermo Fisher Scientific, Waltham, MA, USA). Surface morphology and topography were examined using a Zeiss Sigma 300 scanning electron microscope (SEM) (Carl Zeiss AG, Oberkochen, Germany). Fourier-transform infrared spectroscopy (FTIR) measurements of the freeze-dried CNDs were conducted on a PerkinElmer 1600 spectrophotometer (PerkinElmer, Inc., Waltham, MA, USA) under vacuum at low temperature. X-ray photoelectron spectra were obtained utilizing a SPECS FlexPS XPS system (SPECS GmbH, Berlin, Germany) equipped with XR 50 dual-anode and FOCUS 500 monochromatic X-ray sources. X-ray diffraction measurements were performed using a PANalytical Empyrean X-ray diffractometer (PANalytical B.V., Germany/Netherlands).

2.2 Plant material

In this study, waste bark material of *Pinus pinea* L. was used. The general appearance of the *Pinus pinea* L. tree used in the study is shown in Fig. 1a, while the bark material evaluated in the research is presented in Fig. 1b.

The *Pinus pinea* L. bark material used in this study was obtained during routine annual maintenance and pruning

Fig. 1 General view of the *Pinus pinea* L. tree used in the study (a) and the waste bark material utilized in the analyses (b).

operations of plantation-grown trees located within the central campus area of Karadeniz Technical University (KTU). The plant materials were supplied as waste biomass generated by the KTU Environmental Maintenance Unit, and no field sampling of natural populations was conducted.

The botanical identification of the plant material was performed by Dr Alper Durmaz (Artvin Çoruh University, Ali Nihat Gökyiğit Botanical Garden Application and Research Center) based on the descriptions provided in Flora of Turkey and the East Aegean Islands.[50,51] The current taxonomic status and nomenclature of the species were confirmed by consulting the Plants of the World Online (POWO) database, the "BizimBitkiler" database, and recent literature.

As the material consisted entirely of plant waste derived from maintenance and pruning activities, it was not collected as a scientific field specimen, and therefore no herbarium voucher specimen was prepared.

2.3 Analytical reagents

Working solutions were prepared by appropriate dilution of the cation standard solution (1000 mg L^{-1}, Merck, Germany). Tap water samples were collected from the laboratory in which the study was conducted. Quinine sulfate (Merck, HPLC grade, ≥99%) and sulfuric acid (Merck, analytical grade, 95–97%) were used for quantum yield determination. For the antioxidant capacity assessments, the following analytical-grade chemicals were utilized: ferrous sulfate heptahydrate ($FeSO_4 \cdot 7H_2O$, Sigma-Aldrich, USA) for FRAP standardization, copper(II) chloride ($CuCl_2$, 10 mM, Merck, Germany), neocuproine (7.5 mM, Sigma-Aldrich, USA), ammonium acetate buffer (NH_4Ac, 1 M, pH 7.0, Riedel-de Haën, Germany) for CUPRAC analysis, and 1,1-diphenyl-2-picrylhydrazyl (DPPH, Sigma-Aldrich, USA) radical solution along with L-ascorbic acid (Merck, Germany) as positive control for radical scavenging evaluation. Ethanol of analytical grade (≥99.8%, Merck, Germany) was employed as the primary solvent throughout all antioxidant assays.

2.4 Preparation of the PP-CNDs

Pine nutshells were initially processed by sieving through a 0.5 mm mesh to remove sand and fine dust particles. The sieved material was then washed with deionized water to remove surface soil and mud residues. Following washing, the shells were dried in a Memmert UF260 laboratory oven at 40 °C. After drying, the shells were ground using a Lavion HC 350 g laboratory mill to reduce particle size.

The ground material was transferred to a 250 mL porcelain crucible, filling approximately two-thirds of the vessel volume. The sample was subjected to pyrolysis in a SFL BS12 2UR high-temperature furnace, with heating applied over a temperature range of 250–400 °C and holding times of 1, 2, and 3 hours to identify optimal synthesis conditions.

The pyrolysis product was ground using a Retsch Grindemix GM 300 mill until particles were reduced to <50 μm. A portion of the ground pyrolysis product (0.3 g) was dispersed in 30 mL of deionized water. The suspension was ultrasonicated for 30 minutes using a Bandelin DT 102H ultrasonic water bath (35 kHz, 100 W).

The resulting suspension was subjected to coarse filtration through blue-band filter paper to remove large particles and solid debris. The filtrate was then centrifuged at 10 000 rpm for 10 minutes using a Hermle Z326K centrifuge. The supernatant obtained after centrifugation was further purified by passing through a 0.22 μm PTFE membrane filter. The final volume was adjusted to 30 mL by adding deionized water. The resulting dispersion was used for photoluminescence characterization and analytical applications. The stock dispersion was stored in darkness to prevent photodegradation.

For antioxidant activity measurements, sample solutions were prepared following the same procedure; however, the pyrolysis product mass was set at 0.6 g. The synthesis and purification procedures were adapted from carbon nanodot synthesis methodologies reported in the literature, with protocols optimized for *Pinus pinea* bark as the precursor material.[52]

2.5 Interactions of cations with PP-CNDs

Baseline fluorescence characterization was performed by diluting an aliquot of PP-CNDs (2 mL) with deionized water (2 mL) prior to spectral acquisition. To investigate the modulatory effects of cationic species on the photoluminescent behavior of PP-CNDs, a PP-CNDs suspension (2 mL) was exposed to sequential additions of various cations (100 μM), and comprehensive spectroscopic analysis was subsequently conducted. Systematic fluorometric titration experiments were undertaken to elucidate the quantitative dose–response relationship between cationic concentration and fluorescence intensity modulation. Accordingly, aliquots of PP-CNDs (2 mL) were dispensed into individual reaction vessels, followed by incremental cation supplementation (25–1000 nM), with the total volume adjusted to 4 mL utilizing deionized water. Following a one-minute equilibration interval, the resulting solutions were photoexcited at the predetermined wavelength, and fluorescence emission spectra were subsequently recorded and archived.[52]

2.6 Fluorometric quantification of Fe^{3+} using PP300-3 carbon nanodots

The optical attenuation of PP-CNDs fluorescence initiated by Fe^{3+} ion coordination represents the core principle governing this analytical framework. Fe^{3+} determination in municipal water samples was accomplished utilizing a validated reference standardization protocol. Operationally, PP-CNDs aqueous dispersion (2 mL portions) was deposited into discrete test vessels, whereupon successive increments of Fe^{3+} reference solution were systematically introduced, adjusting the total volume to precisely 4 mL with distilled water. Spectroscopic data acquisition was systematically performed on each sample preparation at the designated excitation wavelength. The established correlation between fluorescence intensity magnitude and Fe^{3+} concentration gradients facilitated the construction of a reference calibration trace. Implementation of this

calibration trace enabled comprehensive quantitative appraisal of Fe^{3+}-enriched municipal water specimens.[52]

2.7 Determination of photoluminescence quantum yield

Carbon nanodots (CNDs) relative fluorescence quantum yield (ϕ_I) determination was performed using quinine sulfate as a standard. The quantum yield of quinine sulfate dissolved in 0.1 M H_2SO_4 medium was reported as 0.54.[53] Solutions of quinine sulfate and CNDs at various concentrations were prepared. The absorption and fluorescence emission spectra of these solutions were recorded under excitation at 330 nm. To determine the slope of the linear plot, the absorption values measured at 330 nm were placed on the horizontal axis, while the integrated intensity (area) of the fluorescence emission spectrum was placed on the vertical axis. The quantum yield was subsequently calculated using eqn (1):

$$\phi_I = \phi_R(m_I/m_R)(\eta_I^2/\eta_R^2) \quad (1)$$

In this equation, ϕ_I and ϕ_R symbolize the quantum yield values for the CNDs and quinine sulfate, respectively. The parameter m_I denotes the gradient of the fitted line for the CNDs, whereas m_R represents the gradient for the standard compound. The variable n corresponds to the refractive index of the solvent medium. The refractive index assigned to quinine sulfate is 1.33, which is identical to the refractive index of the CNDs dispersed in deionized water.

2.8 Determination of antioxidant properties of PP-CND

2.8.1 Determination of total antioxidant capacity *via* iron(III)-TPTZ complex reduction. The antioxidant capacity present in the PP300-3 specimen was quantified employing a spectrophotometric assay based on the reductive transformation of iron(III)-tripyridyltriazine complex by antioxidant substances.[54] The fundamental mechanism of this assay involves the conversion of a yellow Fe^{3+}-TPTZ complex into a blue Fe^{2+}-TPTZ complex when antioxidant molecules donate electrons or hydrogen atoms under acidic pH conditions; the extent of this color transition directly correlates with the total antioxidant activity within the sample. For the analytical execution, 100 μL of the PP300-3 extract (or extraction solvent as blank reference) was combined with 3 mL of FRAP reagent solution and placed in reaction vessels. The mixture was incubated at a constant temperature of 25 °C, and continuous absorbance monitoring was performed at 593 nm over a 4 minute measurement interval. The resulting absorbance data were compared against a standard calibration curve established using ferrous sulfate heptahydrate ($FeSO_4 \cdot 7H_2O$) solutions spanning 100–1000 μmol L^{-1} concentration range. Triplicate measurements were performed for all samples, and the final antioxidant capacity values were calculated and reported as $FeSO_4 \cdot 7H_2O$ equivalents normalized to the dry weight of plant material (μmol g^{-1}).

2.8.2 Evaluation of Cu^{2+}-based antioxidant potential using neocuproine complexation. The antioxidant characteristics of the PP300-3 sample were assessed *via* the CUPRAC methodology, which operates on the principle of Cu^{2+} reduction to Cu^{+} in the presence of antioxidant compounds.[55] This colorimetric detection system utilizes neocuproine, a 1,10-phenanthroline analog, as a chelating agent for the chromogenic quantification of copper(I) formation. The experimental protocol required the combination of three reagent components: copper(II) chloride (10 mM), neocuproine in ethanol (7.5 mM), and ammonium acetate buffer (1 M, pH 7.0). To this prepared reagent system, 0.2 mL of the PP300-3 extract was introduced, and 0.9 mL of deionized water was added to establish a total reaction volume of 4.1 mL. The sample tubes were maintained under ambient temperature conditions in static mode for 60 minutes to permit complete reaction progression. Upon completion of the incubation period, spectrophotometric measurements were taken at 450 nm wavelength. The antioxidant potential was then calculated and expressed in terms of Trolox equivalent antioxidant capacity (TEAC), with results standardized per gram of dry sample material.

2.8.3 Free radical neutralization competency *via* DPPH radical sequestration assay. The capacity of the PP300-3 extract to neutralize free radicals was determined utilizing a 1,1-diphenyl-2-picrylhydrazyl (DPPH) radical scavenging protocol, an established spectrophotometric technique for quantifying antioxidant potency.[56] The mechanistic principle of this assay is grounded in the ability of antioxidant substances to donate electrons or hydrogen atoms to DPPH radicals, causing a reduction in radical concentration and a corresponding decrease in absorbance measurable at 517 nm. For the experimental design, the PP300-3 extract was prepared as a series of sequential serial dilutions encompassing a range of concentrations, with each dilution combined at stoichiometric ratios with an ethanolic DPPH solution. The resulting reaction mixtures were incubated under darkness at room temperature for a predetermined duration to facilitate complete interaction between the antioxidant molecules and DPPH radical species. Following the incubation period, spectrophotometric absorbance readings were obtained at 517 nm wavelength, with ethanol serving as the baseline control. The degree of DPPH radical inhibition was calculated from the differential absorbance between the control and sample-treated solutions. By constructing a linear regression relationship between the extract concentration values and their corresponding DPPH inhibition percentages, the extract concentration producing 50% reduction of initial DPPH radical levels was determined and designated as the IC_{50} parameter. L-Ascorbic acid functioned as a positive reference standard for comparative evaluation of radical scavenging efficiency. Reduced IC_{50} numerical values denote enhanced free radical neutralization capacity, with final results expressed as micrograms per milliliter (μg mL^{-1}).

3 Results and discussion

3.1 Synthesis and characterization of PP-CND

The quantum yield of the CND solution prepared in aqueous medium was calculated by comparing the fluorescence

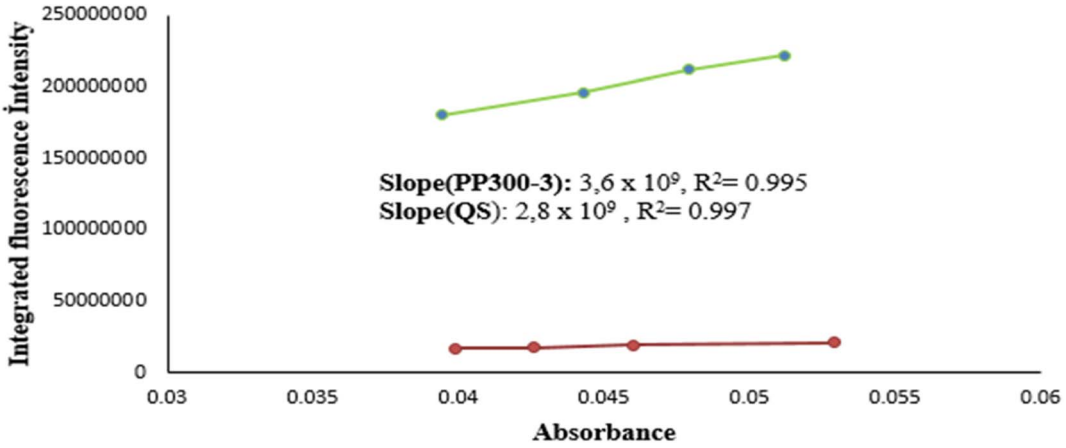

Fig. 2 Integrated fluorescence intensities *versus* absorbance to determine quantum yield. PP300-3 (red), quinine sulfate (green). λ_{ex}: 320 nm.

spectrum area of quinine sulfate used as a reference material, following the method specified in the literature.[57,58] The relevant graphs for PP300-3 are shown in Fig. 2. The quantum yield of the CND was calculated as 3.8%. The wavelengths used in the calculation of quantum yield were selected through optimization for analytical studies. The literature suggests that CNDs with high quantum yield generally exhibit fluorescence emission independent of the excitation wavelength. In contrast, CNDs prepared at higher pyrolysis temperatures tend to have low quantum yield, and the fluorescence emission of these CNDs shows variation with excitation wavelength.[59] The findings regarding the fluorescence properties obtained in this study generally show agreement with the results reported in the literature.[59,60]

A straightforward synthesis procedure utilizing oven-based pyrolysis was implemented for the preparation of carbon nanodots (CNDs). The temperature and temporal parameters employed in the pyrolysis operations are presented in Table 1. However, under certain conditions outlined in Table 1, no suitable pyrolysis product could be obtained. Specifically, during the thermal treatment at 1 and 2 hours, incomplete carbonized residues were observed, preventing the achievement of complete carbonization. When examining the 3 hour pyrolysis processes, partial carbonization occurred in the PP250-3 sample, while PP350-3 exhibited localized white ash formation. Based on these observations, complete carbonization was found to occur exclusively in the PP300-3 sample. Consequently, this particular pyrolysis product was selected and utilized for the preparation of aqueous CND solutions, and all subsequent experimental work proceeded with this optimized CND material.

Table 1 Name of CNDs and the temperature and time used for pyrolysis processes

CNDs	Temperature °C	Time (h)
PP250-1	250	1
PP250-2	250	2
PP250-3	250	3
PP300-1	300	1
PP300-2	300	2
PP300-3	300	3
PP350-1	300	1
PP350-2	300	2
PP350-3	300	3

Comprehensive characterization of the CNDs requires the application of several additional analytical techniques and methods. The specific characterization methodologies employed and their corresponding objectives are presented in Table 2.

To determine the optical properties of the synthesized carbon nanodots (CNDs), UV-Vis and fluorescence spectroscopies were employed. 2 mL aliquot of the stock aqueous CND solution was diluted with deionized water to a final volume of 4 mL, resulting in a 1 : 1 aqueous dilution. The UV-Vis absorption spectrum of this diluted solution is presented in Fig. 3 and reveals important information about the optical characteristics of the material.

The UV-Vis absorption spectrum of PP300-3 carbon nanodots exhibits a broad absorption band beginning at 200 nm and extending into the visible region. Subtle inflection points are observed around 220 nm and 280 nm wavelengths, which reflect the contribution of different electronic transitions. Specifically, $\pi \rightarrow \pi^*$ electronic transitions from aromatic C=C bonds dominate the 200–250 nm region with strong absorption intensity, while $n \rightarrow \pi^*$ transitions from surface C=O functional groups contribute to absorption in the 250–350 nm region. The overlap of these two distinct electronic transition types results in a continuous and broad absorption band spanning the 200–400 nm range, rather than two separate resolved peaks.[61–64] This characteristic absorption profile provides evidence of the π-electron system presence in the heteroatom-containing carbon nanodot structure and confirms surface functionalization. The observed absorption data are consistent with literature reports and originate from π-electronic transitions between sp^2-hybridized carbon atoms and heteroatom-containing surface functional groups.[65]

Under normal visible light conditions, the sample displayed a homogeneous appearance with no apparent luminescence

Table 2 Methods used in the characterisation of CDs and the purpose of these methods

Method	Intended use
SEM analyses	Determination of the morphology of materials at the micro scale
XPS	To determine the surface elemental composition of materials
HRTEM measurements	Determining whether materials are crystalline or amorphous at the nanoscale
XRD	To obtain information about the crystalline structure of materials
FTIR	Determining the types of chemical bonds in the structure of materials
UV-Vis spectroscopy	Determination of the light absorption properties of materials
Fluorescence spectroscopy	Determination of the multicolour properties and fluorescence quantum yields of materials

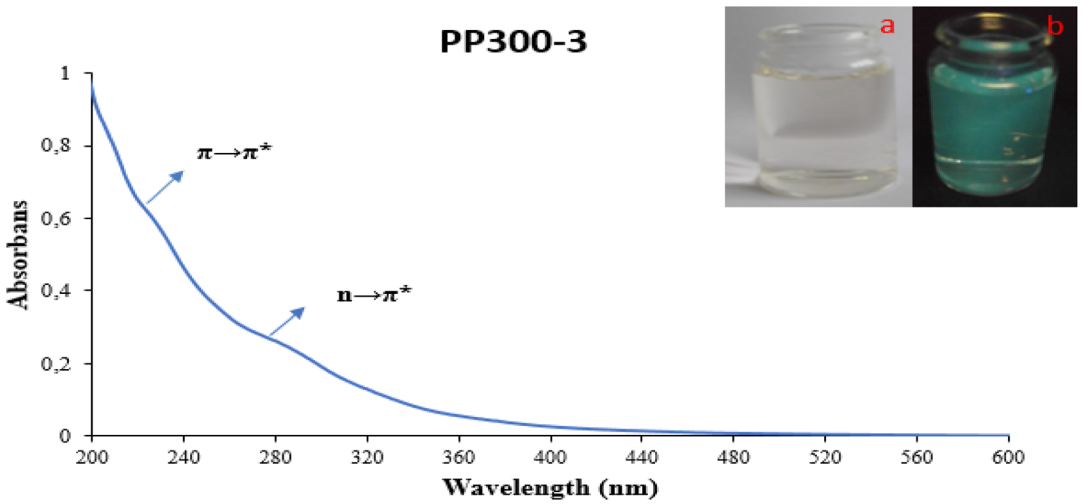

Fig. 3 Photoluminescent properties of PP300-3 carbon nanodots: (a) images of the nanodots under daylight and (b) under UV light at 365 nm.

(Fig. 3a). However, under 365 nm irradiation, bright green fluorescence was clearly observed (Fig. 3b). This observation directly demonstrates that the synthesized carbon nanodots absorb ultraviolet light and emit visible light, thereby confirming their characteristic photoluminescence properties and providing evidence of successful carbon nanodot synthesis.

The SEM image in Fig. 4 (magnification: 1 000 00×; scale bar: 100 nm) reveals that the synthesized carbon dots exhibit heterogeneous surface morphology. The image clearly shows dispersed spherical nanoparticles along with densely aggregated, stacked clusters. The size heterogeneity of the particles and the rough surface structure demonstrate the effectiveness of the pyrolysis synthesis method in producing carbon nanodots with variable morphologies and controlled aggregation patterns.

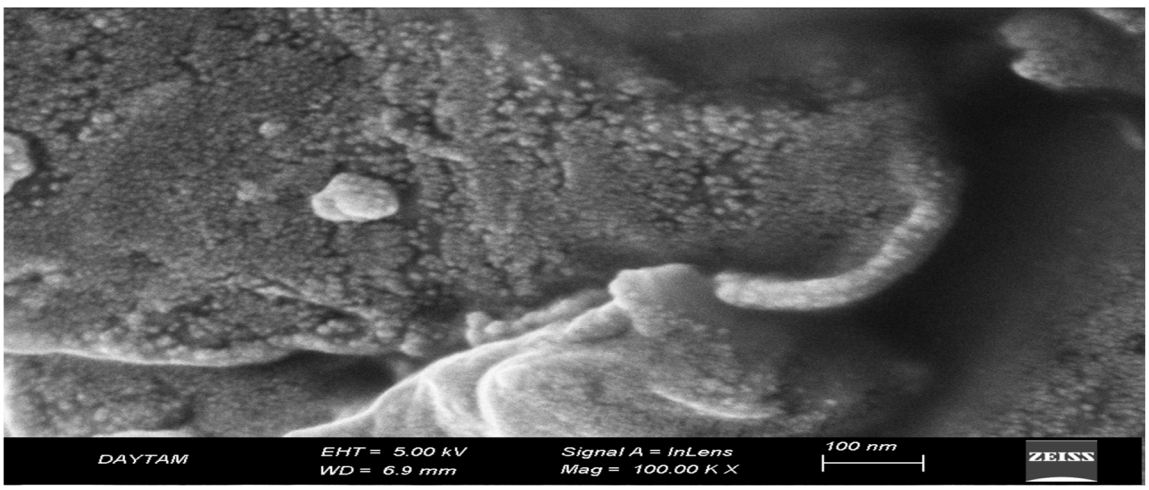

Fig. 4 Scanning electron microscopy (SEM) image of PP300-3 carbon nanodots.

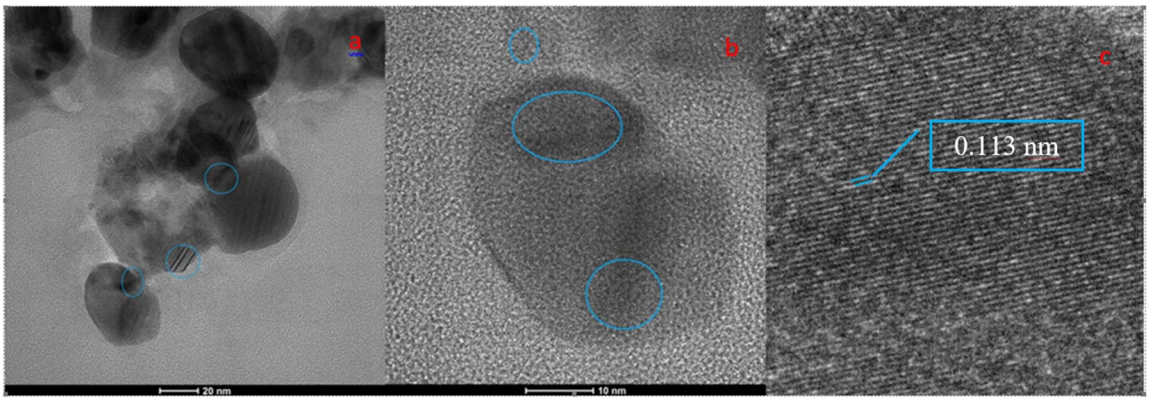

Fig. 5 High-resolution transmission electron microscopy (HRTEM) images of PP300-3 carbon nanodots.

High-resolution transmission electron microscopy (HRTEM) images were obtained at different magnifications to elucidate the crystal structure of the carbon nanodots (Fig. 5a and b, scale bars: 20 nm and 10 nm). Fig. 5a (scale bar: 20 nm) reveals the aggregated state of particles with oval morphology and variable sizes. In regions marked with blue circles, particle overlap and accumulation in specific areas are observed. The literature reports that carbon nanodots produced by pyrolysis methods generally exhibit good dispersibility.[66] However, it has been recently reported that aggregated carbon nanodots can display enhanced fluorescence properties through the aggregation-induced emission enhancement (AIEE) effect. The high-resolution HRTEM image (Fig. 5b, scale bar: 10 nm) clearly demonstrates this heterogeneous structure. While amorphous carbon regions are observed in some areas of the aggregated particles, regular graphite-like crystalline planes form in other regions marked with blue circles. The formation of these ordered planes from multiple crystalline layers indicates the presence of a polycrystalline structure.[67] In Fig. 5c, software-assisted magnification of the crystalline region within the blue circles shown in Fig. 5b makes the periodic structure of graphite-like carbon layers and well-defined lattice fringes more distinct. In these crystalline regions, the distance between planes was directly measured using ImageJ software and determined to be $d = 0.113$ nm.

The XRD diffractogram of the pyrolysis product carbon nanoparticles reveals two characteristic peaks (Fig. 6). The first peak is located at $2\theta = 14.9°$, with a calculated d-spacing value of 5.94 Å. This peak does not match standard graphite planes, indicating the presence of amorphous carbon regions and partially organized carbon domains within the structure. The second peak is observed at $2\theta = 24.36°$, with a d-spacing value determined to be 3.65 Å. This peak corresponds to the characteristic (002) plane of graphite crystals. Compared to the $d_{(002)}$ value of 3.35 Å for standard graphite, an expansion of 0.30 Å is observed. This expansion arises from the nanometer-scale dimensions and limited crystalline size of the carbon dots. No higher-order peaks are observed above 30° in the spectrum. The combined presence of these two peaks demonstrates that the pyrolysis process transforms the organic precursor into a carbon material with a heterogeneous structure comprising crystalline (002) planes and amorphous regions. This structural finding shows significant agreement with the HRTEM images. Indeed, the HRTEM observations in Fig. 5b and c confirm the coexistence of crystalline graphite (002) planes and amorphous regions identified by XRD. The hybrid structure revealed by XRD is consistent with the spatial distribution of polycrystalline

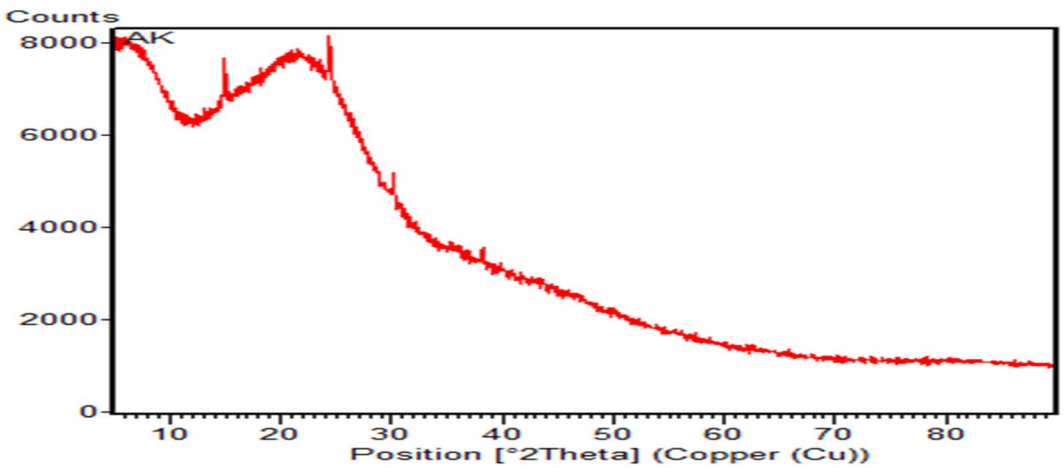

Fig. 6 XRD characterization of crystal structure of PP300-3 carbon nanodots.

graphite layers and amorphous areas observed in HRTEM. This structural configuration indicates that the transformation occurring during the pyrolysis process has successfully generated a sophisticated nanomaterial in which crystalline and amorphous carbon regions coexist from the organic structure. In conclusion, XRD and HRTEM analyses provide complementary information, serving as evidence that the carbon nanoparticles are formed in a controlled manner and constitute a multicomponent carbon system.

Raman spectroscopy analysis was performed to determine the defect density in the carbon structure of the material (Fig. 7). Three characteristic bands are observed in the Raman spectrum: the D band (~1378 cm^{-1}) indicates defects and amorphous regions in the carbon structure, the G band (~1578 cm^{-1}) represents sp^2 hybridized carbon atoms (graphitic character), and the 2D band (~2949 cm^{-1}) indicates the lamellar layer structure. The I(D)/I(G) ratio was determined to be 0.86. The high I(D)/I(G) ratio (0.83) revealed in the Raman spectroscopy findings supports this heterogeneous structure and high defect density. Indeed, the HRTEM observations in Fig. 3b and c confirm the coexistence of crystalline graphite (002) planes and amorphous regions identified by XRD. The Raman analysis shows that the defects indicated by the D band (~1378 cm^{-1}) and the sp^2 carbon character demonstrated by the G band (~1578 cm^{-1}) are in complete agreement with the coexistence of crystalline and amorphous regions observed in HRTEM.

This high I(D)/I(G) ratio of 0.83 indicates a high degree of defect density and amorphous carbon dominance in the material. The high intensity of the D band is in complete agreement with the nanometer-scale defective crystalline structure measured at 0.113 nm in HRTEM and the absence of peaks above 30° in XRD. The high defect density disrupts the crystalline structure of the 002 plane (0.365 nm) observed in XRD, transforming it into nanometer-scale narrow and defective local structures. Thus, Raman analysis integrates the HRTEM and XRD findings, elucidating the heterogeneous amorphous-crystalline structure of the material and its high defect levels. The hybrid structure revealed by XRD (0.365 nm d-spacing), the locally narrow crystalline structure measured in HRTEM (d = 0.113 nm), and the high defect density identified by Raman (I(D)/I(G) = 0.83) demonstrate that these crystalline regions are isolated within an amorphous carbon matrix and that nanoscale ordered lattice structures are surrounded by defective regions. The lattice fringes observed in HRTEM and the lamellar layer structure indicated by Raman's 2D band (~2949 cm^{-1}) collectively confirm the presence of polycrystalline graphite layers. In conclusion, XRD, HRTEM, and Raman spectroscopy analyses provide complementary information, demonstrating that the carbon nanoparticles possess a heterogeneous crystalline-amorphous structure in which nanometer-scale defective polycrystalline graphite regions are dispersed within an amorphous carbon matrix. The local crystalline structure of d = 0.113 nm measured in HRTEM represents the nanometer-scale manifestation of the 002 plane (d = 0.365 nm) identified in XRD, and Raman's high I(D)/I(G) ratio (0.83) reflects the defect density and amorphous content of this structure. This sophisticated heterogeneous structure was formed in a controlled manner from the organic precursor during the pyrolysis process, creating a multicomponent nanomaterial in which crystalline and amorphous carbon regions coexist.

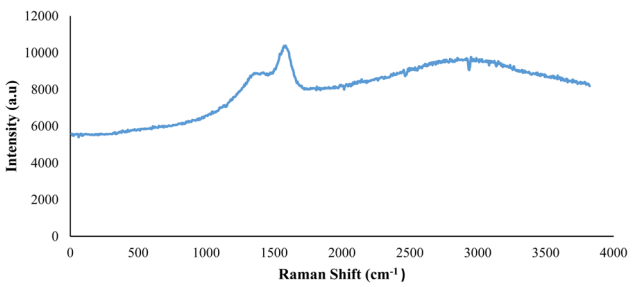

Fig. 7 Raman spectroscopy of PP300-3 carbon nanodots.

Examination of the infrared (IR) spectra of the obtained carbon dots (Fig. 8) reveals a broad peak at 3328 cm^{-1} attributed to O–H stretching vibrations. The peak at approximately 2939 cm^{-1} represents C–H stretching vibrations, while the peak at 1610 cm^{-1} corresponds to C=C stretching vibrations. The peak observed at 1359 cm^{-1} is assigned to bending vibrations of C–H and O–H bonds, and the peak located at 1040 cm^{-1} is attributed to C–O stretching vibrations. These results demonstrate the presence of oxygen-containing functional groups such as OH and C–O on the surface of the graphite-like structure of the carbon dot.

X-ray photoelectron spectroscopy (XPS) analysis was performed to determine the elemental composition and surface chemistry of the material (Fig. 9). The survey XPS spectrum revealed the presence of carbon, nitrogen, oxygen, and trace amounts of silicon. Carbon (81.73%) and nitrogen-oxygen (15.55%) are the dominant elements, with other components comprising less than 4% (Fig. 9a). This high carbon content confirms that the pyrolysis process successfully accomplished carbonization and validates the presence of C–C, C=C, and C–O bonds in the graphenic structure. The oxygen content being the second most abundant element originates from OH groups bound to the structure, and this finding shows consistency with the O–H stretching vibration at 3328 cm^{-1} observed in the IR spectrum.

High-resolution XPS spectra of the carbon and oxygen regions (C 1s and O 1s) were examined for detailed analysis (Fig. 9b and c). Peaks observed in the C 1s spectrum at the 282–284 eV range represent C–C, C=C, and C–O bonds in the graphitic layer (Fig. 9b).[68] Peaks observed in the O 1s spectrum at the 529–532 eV range indicate the presence of surface-bound OH groups, C–O, and C=O bonds (Fig. 9c).[69] These findings show significant agreement with the IR results and demonstrate that oxygen-containing functional groups are widely distributed within the structure. In conclusion, when the IR and XPS spectroscopic analyses are evaluated together, it is determined that although the primary component of the prepared carbon dots is carbon, the material consists of heterogeneous carbon nanomaterial containing oxygen-containing functional groups within its structure and surface.

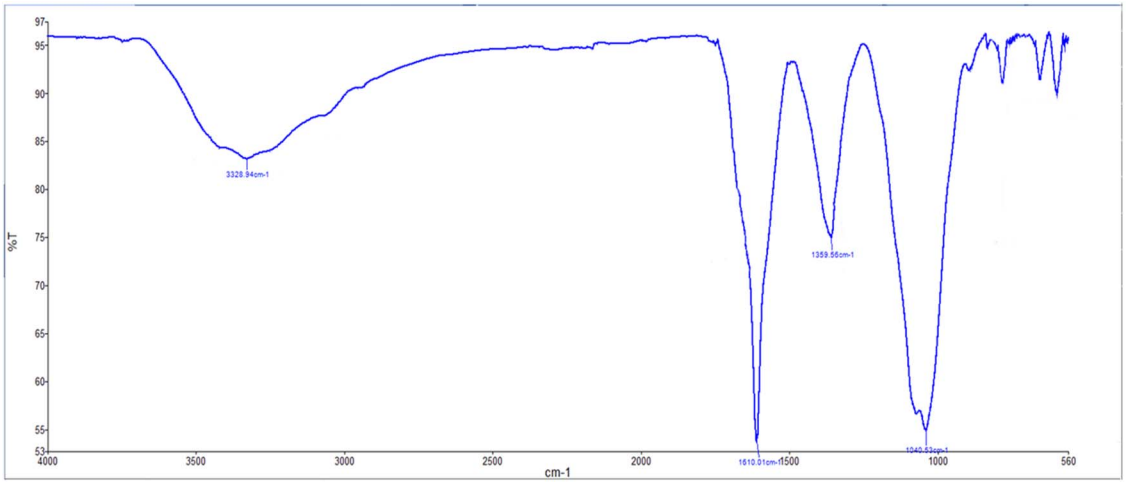

Fig. 8 FTIR spectrum of surface functional groups of PP300-3 carbon nanodots.

The synthesized carbon dots were examined through various analytical techniques. SEM images revealed that the particles exhibited an aggregated structure; HRTEM demonstrated that this structure comprised crystalline graphite layers and amorphous carbon regions; XRD confirmed the presence of the characteristic graphitic (002) plane; and IR and XPS spectroscopy revealed the surface OH and C–O functional groups. All these results show consistency with one another. Due to these oxygen-containing functional groups, the carbon dots acquired the capability to absorb ultraviolet light and emit visible light (photoluminescence). In conclusion, carbon dots produced from tree bark *via* the pyrolysis method constitute a nanomaterial with a controlled structure and high optical properties.

3.2 Fluorescence properties of CNDs

The fluorescence properties of the carbon nanodot (PP300-3) were systematically investigated by recording emission spectra at different excitation wavelengths in the range of 300–400 nm.

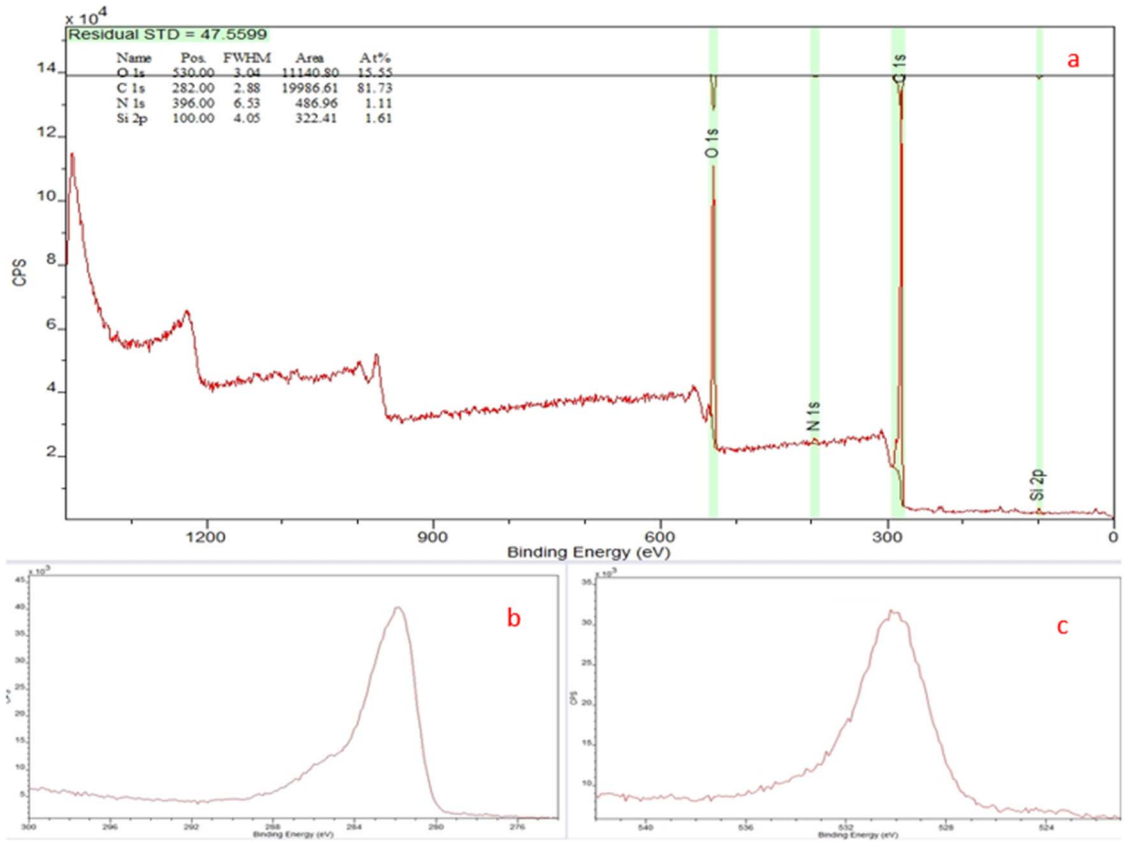

Fig. 9 XPS analysis of PP300-3 carbon nanodots: (a) XPS survey spectrum, (b) C 1s spectrum, and (c) O 1s spectrum.

Şekil 10′de gösterilen spektrumlar PTI QM-4 spektrofluorimetresi kullanılarak (1.0 nm slit width, 600V PMT, 0.05 s integration time, 25 ± 1 °C) kaydedilmiştir. As shown in Fig. 10a, the carbon nanodot exhibits a pronounced excitation-wavelength-dependent fluorescence behavior. With increasing excitation wavelength, a gradual bathochromic shift in the emission maximum accompanied by a decrease in fluorescence intensity was observed. This optical behavior is consistent with previously reported characteristics of carbon nanodots in the literature[70] and reflects the multicolor photoluminescence nature typical of such nanomaterials.

Comparative analysis with previously reported studies indicates that the fluorescence behavior is dependent on the carbonization temperature. While carbon nanodots synthesized at lower carbonization temperatures (150 °C) exhibit excitation-independent emission spectra, samples obtained at higher pyrolysis temperatures (300 °C) show excitation-dependent fluorescence behavior accompanied by a progressive decrease in intensity.[71]

In the present study, the carbon nanodot synthesized under the applied pyrolysis conditions exhibits a pronounced excitation-dependent fluorescence behavior over the entire investigated excitation wavelength range. The highest fluorescence intensity was obtained at an excitation wavelength of 320 nm, and under this excitation condition, the emission maximum was determined to be at 432 nm (Fig. 10b).

3.3 The interaction of CNDs with cations

Carbon nanodot (CND) solutions were synthesized according to the prescribed protocol for analytical applications, and the experimental parameters were optimized accordingly. The

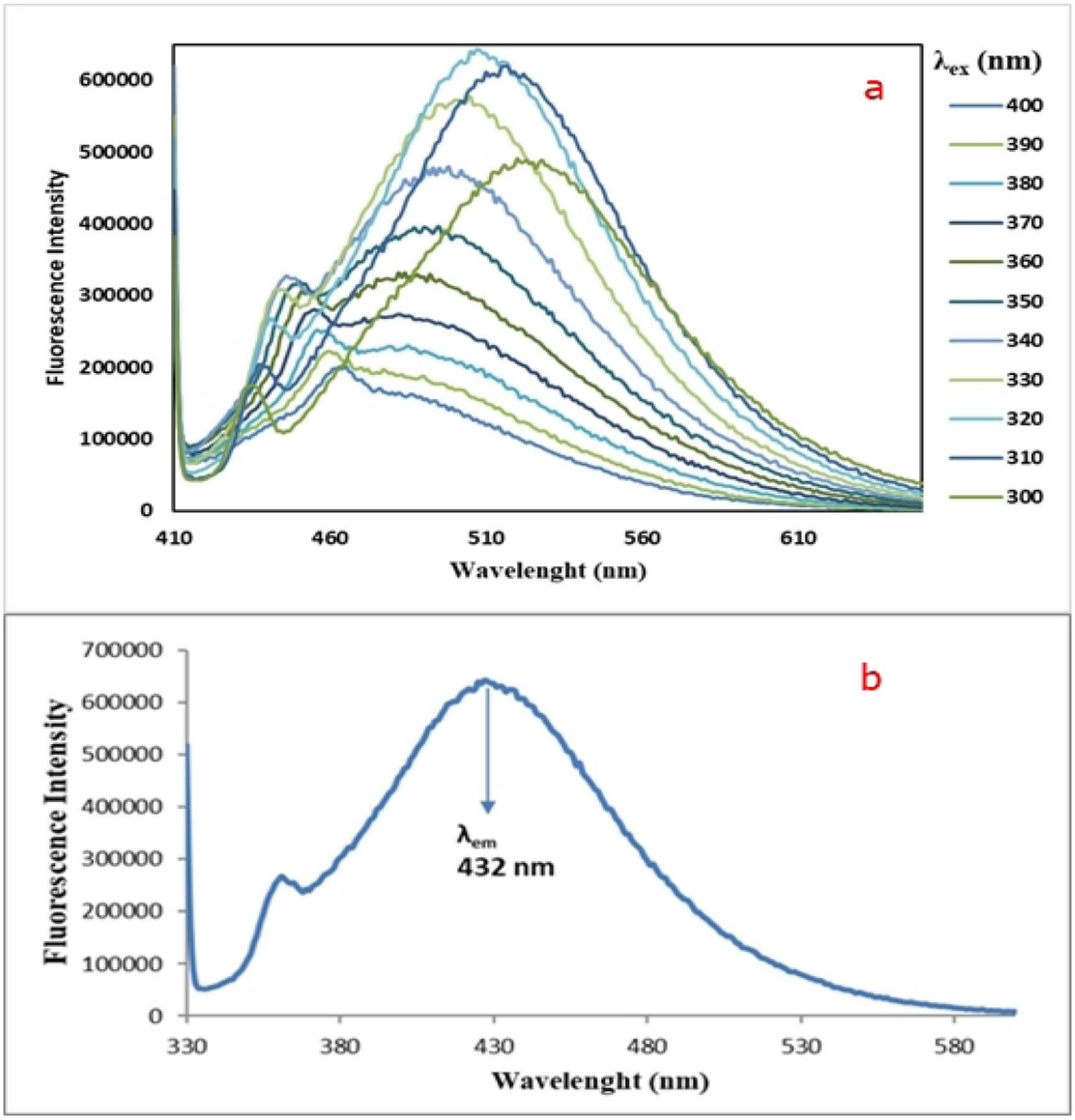

Fig. 10 Excitation-wavelength-dependent fluorescence of PP300-3 carbon nanodots: (a) spectra, and (b) intensity at 320 nm showing emission at 432 nm.

fluorescence behavior of the resultant CND in aqueous medium was systematically investigated in the presence of 33 metal cations, namely Fe^{3+}, Sb^{3+}, Ba^{2+}, Ni^{2+}, Cr^{3+}, Mg^{2+}, Pd^{2+}, Zn^{2+}, Sn^{4+}, Al^{3+}, Mn^{2+}, Pb^{2+}, V^{5+}, Bi^{3+}, Cu^{3+}, Y^{3+}, Ti^{4+}, Ca^{2+}, Ag^{+}, W^{6+}, Li^{+}, Pt^{2+}, Tl^{+}, Mo^{6+}, Sc^{3+}, Rb^{+}, As^{3+}, Na^{+}, K^{+}, Co^{2+}, Au^{3+}, Cd^{2+}, and Se^{4+}, with the corresponding results presented in Fig. 11. Metal cation screening experiments were performed using PTI QM-4 spectrofluorimeter (1.0 nm slit width, 600V PMT, 0.05 s integration time, 25 ± 1 °C) at 320 nm excitation wavelength. To facilitate visual discrimination of the fluorescence intensity alterations induced by the respective cations, the data were rendered in columnar graph format as illustrated in Fig. 11b. Comprehensive screening revealed that Au^{3+}, Bi^{3+}, Pd^{3+}, Pt^{2+}, and Fe^{3+} cations elicited the most pronounced perturbations in the fluorescence characteristics of the CND, thereby warranting further investigation of their quantitative determination utilizing CND-based analytical methodologies.

Spectrofluorometric titration experiments were subsequently performed with the aforementioned metal ions to elucidate the existence of a linear correlation between increasing cation concentration and fluorescence intensity. The results demonstrated that only Fe^{3+} ions exhibited a predictable, concentration-dependent fluorescence response among the five cations evaluated. On the basis of these findings, appropriate calibration curves were constructed to develop a spectrofluorometric assay, which was subsequently validated through the analysis of municipal water samples.

3.4 Fluorometric determination of Fe^{3+} using PP300-3 carbon nanodots

In spectrofluorometric titration studies of PP300-3, Fe^{3+} was identified as the most suitable metal ion. Comprehensive screening of 33 different metal cations revealed that Fe^{3+} ions exhibited the most pronounced reduction (%92) in the fluorescence characteristics of PP300-3. This selective quenching behavior of Fe^{3+} originates from its coordination to oxygen-containing functional groups (OH, C=O) on the nanodot surface. During photoexcitation, electrons bound to Fe^{3+} are quenched through an electron transfer mechanism, resulting in fluorescence loss. Although four other metal ions (Au^{3+}, Bi^{3+}, Pd^{2+}, Pt^{2+}) exhibited significant quenching, only Fe^{3+} demonstrated a linear fluorescence response dependent on concentration. The linear response exhibited by Fe^{3+}, as opposed to the irregular quenching observed with other metal ions, suggests that Fe^{3+} forms reproducible and homogeneous interactions with the carbon nanodot surface functional groups. This behavior is consistent with Fe^{3+}'s coordination chemistry and enables the reliable quantitative determination.This linear dose–response relationship and high selectivity make Fe^{3+} an ideal target element for spectrofluorometric determination. As demonstrated in Fig. 12, the fluorescence spectrum of PP300-3

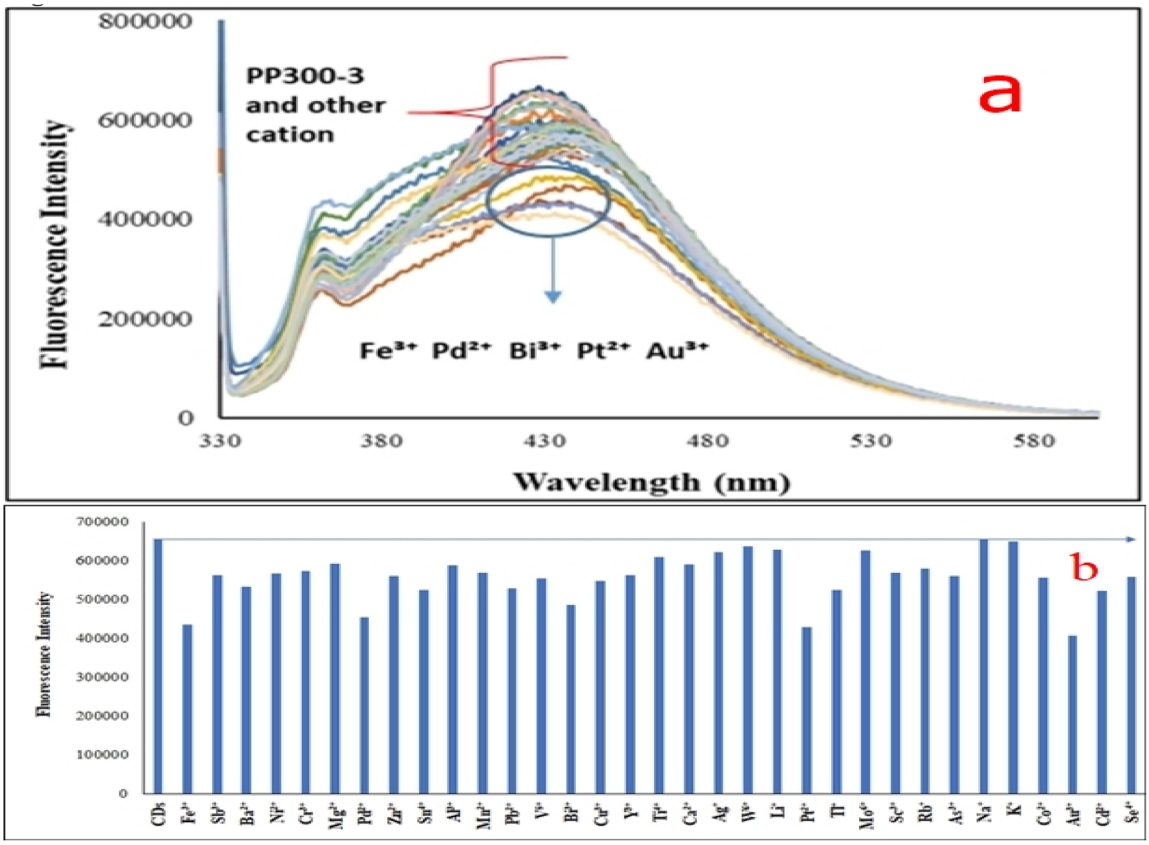

Fig. 11 Interaction of PP300-3 with metal cations.

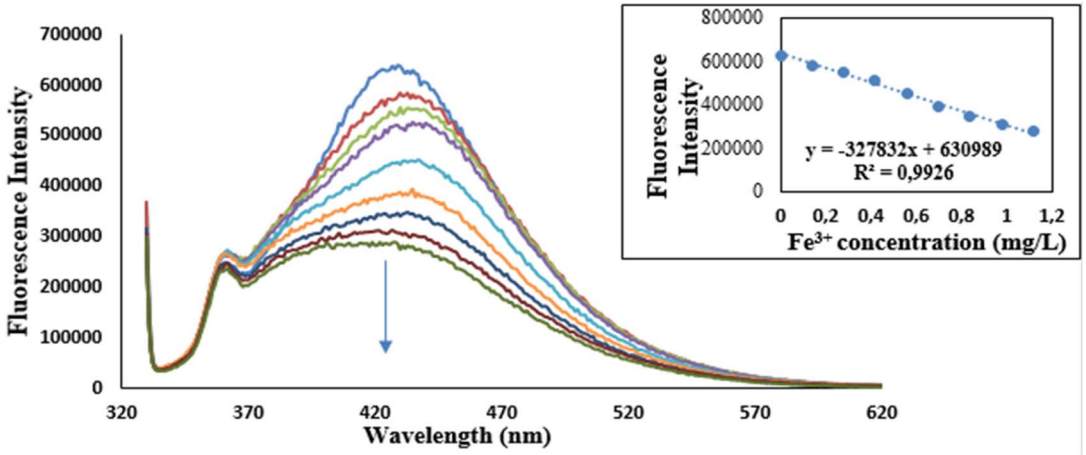

Fig. 12 Fe^{3+} determination and calibration curve.

exhibited a regular quenching phenomenon across a broad wavelength range with increasing Fe^{3+} concentration. The inset panel of the figure explicitly displays the variation in fluorescence intensity at 320 nm as a function of increasing iron concentration. Upon examination of these results, a robust linear correlation was established between Fe^{3+} concentration and fluorescence intensity within the 0–1.11 mg L^{-1} range.

The proposed analytical methodology furnishes significant advantages in analytical chemistry applications by virtue of its simplicity and expediency in the measurement procedure. The reliability and accuracy of the method were systematically assessed by spiking tap water samples with Fe^{3+} standard solutions of predetermined concentration. Through these spike-recovery studies, the analytical performance and measurement sensitivity of the proposed method were comprehensively validated.[72] The performance data demonstrating the analytical capability of the procedure, together with all operational parameters, are presented in comprehensive detail in Table 3.

The analytical figures of merit presented in Table 3 were calculated according to ICH Q2(R1) international validation guidelines. Limit of detection (LOD) and limit of quantification (LOQ) were determined using the equations LOD = 3 × SD/m and LOQ = 9 × SD/m, where SD represents the standard deviation of 11 blank measurements and m is the slope of the external calibration curve (ECM). Precision was assessed from N = 12 (intra-day) and N = 21 (inter-day) replicate measurements at 25 ± 1 °C. Accuracy was determined through spike-recovery studies at three concentration levels (N = 12 each), with all recovery values within the 95–105% range. The excellent coefficient of determination (R^2 = 0.9926) demonstrates the reliability of the external calibration method for Fe^{3+} quantification over the 0–1.1 mg L^{-1} range.

3.5 Antioxidant potential of PP300-3 carbon dot: complementary analysis using FRAP, CUPRAC, and DPPH methods

In order to determine the antioxidant potential of the PP300-3 carbon dot, analyses based on three different redox methods were performed on its stock aqueous solution. This

Table 3 Analytical performance data of the recommended method for Fe^{3+} quantification in tap water using PP300-3 under 320 nm excitation wavelength

Excitation wavelength (nm)	320
Emission wavelength (nm)	432
Limit of detection (LOD) (mg L^{-1})	0.035
Limit of quantification (LOQ) (mg L^{-1})	0.107
Linear dynamic range (mg L^{-1})	0–1.1
Fluorescent reagent	(1/10) seyreltilmiş stok FK315-3 çözeltisi
Reagent volume (mL)	2
Total volume (mL)	4
Solvent medium	Su
Pre-measurement incubation time	1–2 dk
Coefficient of determination (R^2)	0.9926
Calibration	ECM (external calibration method)
Spiked (mg L^{-1})	0.279
RSD% (Intra-day precision)	1.97
RSD'% (Inter-day precision)	1.65
R% (Intra-day recover)(N = 12)	99.56
R% (Inter-day recovery)(N = 21)	99.35

comprehensive evaluation was designed to elucidate the various antioxidant mechanisms of the sample.

Following the application of the FRAP method, the PP300-3 carbon dot demonstrated a reducing potential of 3.48 ± 0.51 μmol $FeSO_4 \cdot 7H_2O$ E g^{-1} (Table 4). In this assay, the Fe^{3+}-TPTZ complex was reduced to its Fe^{2+} form by the carbon dot, and the resulting increase in absorbance at 593 nm was measured spectrophotometrically. The obtained value serves as a quantifiable indicator of the sample's electron-donating capacity relative to the standard reference.

The CUPRAC assay revealed that the carbon dot exhibited antioxidant activity at a level of 18.35 ± 0.20 μmol Trolox E g^{-1} (Table 4). The 2,9-dimethyl-1,10-phenanthroline (neocuproine) employed in this assay plays a pivotal role in chelating Cu^{2+} ions and facilitating the measurement of antioxidant capacity. The carbon dot reduced Cu^{2+} to Cu^{+}, which subsequently formed a chelate complex with the neocuproine ligand; the absorbance of this colored complex at 450 nm was recorded spectrophotometrically. Consistent with the FRAP findings, this result further attests to the pronounced electron-transfer capacity of PP300-3.

To evaluate antioxidant activity from the perspective of radical scavenging, the DPPH assay was employed. The SC_{50} value determined by this method represents the concentration of carbon dot required to neutralize 50% of the 2,2-diphenyl-1-picrylhydrazyl radicals. The PP300-3 sample exhibited an SC_{50} value of 4.36 ± 0.92 mg mL^{-1} (Table 4); the low magnitude of this parameter indicates pronounced antioxidant activity. Consequently, the carbon dot is capable of scavenging half of the DPPH radicals at a concentration of 4.36 mg mL^{-1}.

The results obtained from the aforementioned three methods exhibit complementary characteristics. Whereas the FRAP and CUPRAC assays quantify antioxidant activity through measurement of reducing capacity, the DPPH method delineates the radical-scavenging mechanism. The elevated activity levels demonstrated by PP300-3 across all three disparate redox reactions substantiate its potential as a promising candidate for application in biomedical and pharmaceutical fields.

3.6 Antioxidant comparison: stone pine bark *versus* food-based carbon nanodots

Accumulating evidence in the scientific literature substantiates the utility of biomass-derived carbon nanodots as free radical scavengers. Among pioneering contributions, Pal's group synthesized nanostructures *via* hydrothermal processing utilizing curcumin as a carbon precursor, subsequently functionalized with polyethyleneimine, achieving an EC_{50} measurement of 18.2 μg mL^{-1} in radical capture assays.[73] Nevertheless, curcumin represents an edible compound, and the corresponding synthesis protocol involves extended thermal processing durations. The current work circumvents these limitations by demonstrating the expedient fabrication of antioxidatively competent nanostructures from *Pinus Pinea* L. bark waste through a minimalist synthetic approach, thereby realizing improved economic efficiency and operational convenience.

Parallel investigations across multiple biomass feedstocks have yielded comparable outcomes. Hydrothermally-processed tomato-derived materials demonstrated respectable radical neutralization despite protracted synthesis intervals extending to 6 hours.[27] A distinct approach incorporated pomelo precursors with ammonium persulfate-mediated surface modification, requiring 12 hour heating cycles.[75] Such systems, characterized by nitrogen and sulfur-rich surface chemistry, exhibited pronounced capacity for neutralizing DPPH, hydroxyl, and superoxide species.[74] Coriander leaf-based nanoparticles similarly manifested significant antioxidative capacity *via* analogous hydrothermal routes.[75] Collectively, these earlier studies emphasized edible plant materials as feedstock sources.

Waste stream valorization strategies have gained prominence in recent investigations.[76,77] Coffee residue phenolics (extracted *via* sequential alkali treatment and acid neutralization) yielded nanoparticles with $EC_{50} = 110$ μg mL^{-1} in capacity benchmarking.[76] Coconut shell-derived systems demonstrated comparable efficacy, registering 60 μg mL^{-1} *via* radical absorption measurements.[77]

The distinguishing advantage of the herein-described methodology lies in its elimination of exogenous chemical reagents during fabrication. Utilizing *Pinus pinea* L. bark byproducts as the feedstock, the proposed strategy achieves environmental compatibility, minimal processing duration, and instrumental simplicity (pyrolytic treatment apparatus solely). Resultant nanoparticles demonstrate antiradical performance metrics equivalent to or surpassing literature-documented alternatives, establishing technical and economic viability.

3.7 Comparative study of PP300-3 carbon nanodots in Fe^{3+} analysis

A comprehensive comparison of Fe^{3+} determination methods employing carbon nanodots (CNDs) *via* fluorometric measurements has been conducted in the literature. The analysis of the findings presented in Table 5 reveals noteworthy conclusions regarding the limit of detection (LOD) value (35.43 μg L^{-1}) obtained for Fe^{3+} determination in tap water using the PP300-3 material.[78–81] Although some methods listed in Table 5 possess lower detection limits compared to PP300-3, the

Table 4 Antioxidant properties of PP300-3 carbon dot as determined by FRAP, CUPRAC, and DPPH assays[a]

CD	FRAP (μmol $FeSO_4 \cdot 7H_2O$ E g^{-1})	CUPPAC (μmol Troloks E g^{-1})	DPPH SC_{50} mg mL^{-1}
PP300-3	3.48 ± 0.51	18.35 ± 0.20	4.36 ± 0.92

[a] SC_{50}(Troloks): 0.004 ± 0.000 mg mL^{-1}.

Table 5 Comparison of some of the CNDs used in Fe^{3+} determination in the literature[a]

Sample	LOD	LR	Ref.
Blood serum	1.60–16.6 × 10^{-5} mol L^{-1}	6.05 × 10^{-6} mol L^{-1}	77
Serum and living cells	0.33 μM	1–150 μM	78
DLD cells	56.0 ppb	—	79
BGC-823 and CT26.WT cells	180 nM	0–100 μM	80
Fungal cells, drinking water, and river waters	0.001 μM	0.01–100 μM	81
Lake water	0.025 μmol L^{-1}	1.0–5.0 μmol L^{-1} 5.0–50.0 μmol L^{-1}	82
Tap water	0.03543 mg L^{-1}	0–1.1 mg L^{-1}	This work

[a] LR: linear range, LOD: limit of detection.

development and validation of these methods were conducted on biological matrices such as cell cultures, serum, and cancer cell lines.[78–82] The fact that none of these methods has been applied to real water samples significantly limits their practical applicability in environmental analysis.

In contrast, the PP300-3 method has been successfully applied directly to authentic tap water samples, distinguishing it from conventional laboratory-based studies. The most significant advantage of PP300-3 resides in its synthesis from natural waste *via* bottom-up methodology, yielding a cost-effective and readily scalable material. Furthermore, the utilization of recyclable biomass sources renders PP300-3 environmentally benign and amenable to industrial-scale implementation. Particularly noteworthy is that PP300-3 can be directly deployed on authentic water matrices, providing an operational solution for practical applications such as environmental contamination assessment and drinking water quality assurance beyond the confines of the laboratory. Concurrently, it exhibits good selectivity towards Fe^{3+}, coupled with rapid response kinetics and facile analytical procedures. The synergistic combination of these attributes positions PP300-3 as a practical and valuable instrument for environmental monitoring and aquatic safety surveillance in real-world field applications.

4 Conclusion

In this study, sophisticated carbon nanodots designated as PP300-3 were successfully synthesized utilizing a straightforward and environmentally benign pyrolytic methodology employing *Pinus pinea* L. bark residue as the carbon precursor material. Exhaustive characterization investigations encompassing scanning electron microscopy, high-resolution transmission electron microscopy, X-ray diffraction, Fourier-transform infrared spectroscopy, and X-ray photoelectron spectroscopy unambiguously demonstrated that the synthesized material exhibits a heterogeneous structural configuration consisting of crystalline graphitic layers interspersed with amorphous carbon domains. This distinctive structural characteristic directly determines the material's robust photoluminescent capacity and inherent biological functionality, thereby establishing a direct relationship between structural organization and the material's optical and bioactive properties.

Systematic optical and spectroscopic investigations revealed that PP300-3 manifests pronounced excitation-wavelength-dependent photoluminescence behavior. The attainment of maximum photoluminescence quantum yield efficiency at 320 nm excitation wavelength substantiates the material's exceptional suitability for analytical applications. Comprehensive screening experiments conducted with twenty-three metal cations identified Fe^{3+} ions as the most pronounced fluorescence quenching agent in the PP300-3 system. The spectrofluorometric methodology developed herein, distinguished by its operational simplicity, rapid response kinetics, and good selecti good selectivity vity toward ferric ions, establishes itself as an indispensable analytical tool for environmental contamination assessment and water quality monitoring in authentic aqueous matrices.

The antioxidant potential of the PP300-3 nanomaterial was rigorously investigated utilizing three complementary biochemical assay methodologies—ferric reducing antioxidant power (FRAP), cupric ion reducing antioxidant capacity (CUPRAC), and 2,2-diphenyl-1-picrylhydrazyl (DPPH) techniques. The consistently elevated antioxidative activity observed across all three independent redox-based mechanisms provides compelling evidence that this nanomaterial possesses both substantial electron-transfer capacity and pronounced free radical neutralization competency. Particularly noteworthy is the low SC_{50} value derived from the DPPH assay, which provides definitive evidence that PP300-3 exhibits formidable protective mechanisms against deleterious free radical species.

The fundamental distinguishing feature of this investigation resides in demonstrating that nanomaterials derived from industrial waste materials, while maintaining synthetic simplicity and environmental compatibility, can attain performance metrics equivalent to or surpassing those achieved through elaborate laboratory-developed methodologies. The utilization of recyclable biomass feedstocks, particularly *Pinus pinea* L. bark byproducts, as carbon sources exemplifies a pragmatic strategy toward achieving concurrent economic and environmental sustainability objectives. Significantly, the successful validation of PP300-3 in authentic tap water samples demonstrates its practical applicability and utility extending beyond idealized laboratory conditions, thus confirming its deployment potential in real-world analytical scenarios.

In conclusion, the PP300-3 carbon nanodots presented in this investigation emerge as a promising candidate material for diverse applications encompassing environmental contamination monitoring, potable water quality assurance, and biomedical applications. Subsequent research endeavors would substantially benefit from enhanced optimization of selectivity and analytical sensitivity, mechanistic elucidation of molecular–level interaction pathways, and investigation of therapeutic efficacy in biomedical contexts. Moreover, systematic comparative evaluation of structurally analogous nanomaterials synthesized from alternative biomass sources and under varied pyrolytic conditions would facilitate the establishment of generalized design principles governing this material class, thereby advancing rational design strategies for developing advanced carbon-based nanomaterials for bioanalytical and biomedical applications.

Ethics approval and consent to participate

The plant material used in this study was obtained from waste biomass generated by routine annual maintenance and pruning activities of *Pinus pinea* L. trees located within the central campus area of Karadeniz Technical University (KTÜ). The material was sourced from waste products managed by the KTÜ Environmental Maintenance Unit.

No plant specimens were collected from natural populations, protected habitats, or privately owned lands in this study. Due to the use of maintenance waste generated within the university campus, formal sampling permission, license, or ethical approval was not required. No ethical concerns arise regarding the acquisition of this material.

Author contributions

A. G. was responsible for conceptualization, methodology design, execution of all experiments, data analysis, and manuscript preparation.

Conflicts of interest

The author states that there are no financial or personal conflicts of interest related to this work.

Data availability

All data generated or analyzed during this study are included in this published article.

Acknowledgements

I gratefully acknowledge Dr Alper Durmaz (Artvin Çoruh University, Ali Nihat Gökyiğit Botanical Garden Application and Research Center) for the formal botanical identification of *Pinus pinea* L. bark material used in this study. Furthermore, the author is also thankful to Artvin Coruh University Scientific Research Project Coordination for supporting this research (Project Number: 2024.TAB.F65.02.08).

References

1 Z. L. Peng, X. Han, S. H. Li, A. O. Al-Youbi, A. S. Bashammakh, M. S. El-Shahawi and R. M. Leblanc, Carbon dots: Biomacromolecule interaction, bioimaging and nanomedicine, *Coord. Chem. Rev.*, 2017, **343**, 256–277.
2 S. N. A. Shah and J. M. Lin, Recent advances in chemiluminescence based on carbonaceous dots, *Adv. Colloid Interface Sci.*, 2017, **241**, 24–36.
3 B. Wang and S. Lu, The light of carbon dots: from mechanism to applications, *Matter*, 2022, **5**, 110–149.
4 M. Liu, Optical properties of carbon dots: a review, *Nanoarchitectonics*, 2020, 1–12.
5 Q. Wang, Y. Li, F. Huang, S. Song, G. Ai, X. Xin, B. Zhao, Y. Zheng and Z. Zhang, Recent advances in g-C3N4-based materials and their application in energy and environmental sustainability, *Molecules*, 2023, **28**, 432.
6 Q. Wang, Q. Zhang, H. He, Z. Feng, J. Mao, X. Hu, X. Wei, S. Bi, G. Qin and X. Wang, Carbon dot blinking fingerprint uncovers native membrane receptor organizations via deep learning, *Anal. Chem.*, 2022, **94**, 3914–3921.
7 X. Y. Xu, R. Ray, Y. L. Gu, H. J. Ploehn, L. Gearheart, K. Raker and W. A. Scrivens, Electrophoretic analysis and purification of fluorescent single-walled carbon nanotube fragments, *J. Am. Chem. Soc.*, 2004, **126**, 12736–12737.
8 B. Wang, H. Cai, G. I. Waterhouse, X. Qu, B. Yang and S. Lu, Carbon dots in bioimaging, biosensing and therapeutics: a comprehensive review, *Small Sci.*, 2022, **2**, 2200012.
9 L. M. T. Phan and S. Cho, Fluorescent carbon dot-supported imaging-based biomedicine: a comprehensive review, *Bioinorg. Chem. Appl.*, 2022, **2022**, 9303703.
10 F. Yan, Y. Jiang, X. Sun, Z. Bai, Y. Zhang and X. Zhou, Surface modification and chemical functionalization of carbon dots: a review, *Microchim. Acta*, 2018, **185**, 1–34.
11 G. Leménager, E. De Luca, Y. P. Sun and P. P. Pompa, Super-resolution fluorescence imaging of biocompatible carbon dots, *Nanoscale*, 2014, **6**, 8617–8623.
12 Q. Wang, Z. Feng, J. Mao, L. Liu, X. Chen, X. Wei and H. Fang, Microwavesynthesized fluorescent carbon nanoparticles for nucleolus imaging, *Prog. Biochem. Biophys.*, 2021, **48**, 1204–1213.
13 J. Mao, M. Xue, X. Guan, Q. Wang, Z. Wang, G. Qin and H. He, Near-infrared blinking carbon dots designed for quantitative nanoscopy, *Nano Lett.*, 2022, **23**, 124–131.
14 S. H. Lim, W. Shen and Z. Gao, Carbon quantum dots and their applications, *Chem. Soc. Rev.*, 2015, **44**, 362–381.
15 M. Tuerhong, X. Yang and Y. Xue-Bo, Review on carbon dots and their applications, *Chin. J. Anal. Chem.*, 2017, **45**(1), 139–150.
16 Y. Choi, Y. Choi, O. H. Kwon and B. S. Kim, Carbon dots: Bottom-up syntheses, properties, and light-harvesting applications, *Chem. Asian J.*, 2018, **13**, 586–598.
17 V. S. Sivasankarapillai, A. V. Kirthi, M. Akksadha, S. Indu, U. D. Dharshini, J. Pushpamalar and L. Karthik, Recent

advancements in the applications of carbon nanodots: exploring the rising star of nanotechnology, *Nanoscale Adv.*, 2020, **2**, 1760–1773.
18 L. Cui, X. Ren, M. Sun, H. Liu and L. Xia, Carbon Dots: Synthesis, properties and applications, *Nanomaterials*, 2021, **11**, 3419.
19 B. P. Oliveira and F. O. M. da Silva Abreu, Carbon quantum dots synthesis from waste and by-products: Perspectives and challenges, *Mater. Lett.*, 2021, **282**, 128764.
20 C. Kang, Y. Huang, H. Yang, X. F. Yan and Z. P. Chen, A review of carbon dots produced from biomass wastes, *Nanomaterials*, 2020, **10**, 2316.
21 Y. Jiang, L. Xiao, J. Wang, T. Tian, G. Liu, Y. Zhao, J. Guo, W. Zhang, J. Wang, C. Chen, W. Gao and B. Yang, Carbon nanodots constructed by ginsenosides and their high inhibitory effect on neuroblastoma, *J. Nanobiotechnol.*, 2023, **21**, 244.
22 Q. Zong, H. Chen, Y. Zhao, J. Wang and J. Wu, Bioactive carbon dots for tissue engineering applications, *Bioact Carbon Dots Tissue Eng*, 2024, **5**, 1–14.
23 D. Li, X. Na, H. Wang, Y. Xie, S. Cong, Y. Song, X. Xu, B. W. Zhu and M. Tan, Fluorescent carbon dots derived from maillard reaction products: their properties, biodistribution, cytotoxicity, and antioxidant activity, *J. Agric. Food Chem.*, 2018, **66**, 1569–1575.
24 M. Hou, Q. Li, X. Liu, C. Lu, S. Li, Z. Wang and L. Dang, Substantial Enhancement of the Antioxidant Capacity of an α-Linolenic Acid Loaded Microemulsion: Chemical Manipulation of the Oil−Water Interface by Carbon Dots and Its Potential Application, *J. Agric. Food Chem.*, 2018, **66**, 6917–6925.
25 F. Li, T. Li, C. Sun, J. Xia, Y. Jiao and H. Xu, Selenium-doped carbon quantum dots for free-radical scavenging, *Angew. Chem., Int. Ed.*, 2017, **56**, 9910–9914.
26 V. Ruiz, L. Yate, I. Garcia, G. Cabanero and H. J. Grande, Tuning the antioxidant activity of graphene quantum dots: Protective nanomaterials against dye decoloration, *Carbon*, 2017, **116**, 366–374.
27 A. Saikia and N. Karak, Polyaniline nanofiber/carbon dot nanohybrid as an efficient fluorimetric sensor for As (III) in water and effective antioxidant, *Mater. Today Commun.*, 2018, **14**, 82–89.
28 S. K. Başkaya and M. Çeşme, Synthesis of N-doped carbon quantum dots by hydrothermal synthesis method and investigation of optical properties, *Turk. J. Nat. Sci.*, 2021, **10**, 206–211.
29 S. Dinç and R. Günhan Özmelleş, Carbon dots applications in electrochemical and electrochemiluminescence sensors: Some examples of pathogen sensors, *Turk. J. Chem.*, 2020, **2**, 37–46.
30 J. Zhang and S. H. Yu, Carbon dots: large-scale synthesis, sensing and bioimaging, *Mater. Today*, 2016, **19**, 382–393.
31 R. Das, R. Bandyopadhyay and P. Pramanik, Carbon quantum dots from natural resource: A review, *Mater. Today Chem.*, 2018, **8**, 96–109.
32 S. Dinç and M. Kara, Synthesis and applications of carbon dots from food and natural products: Review, *J. Apit. Nat.*, 2018, **1**, 33–37.
33 P. Zuo, X. Lu, Z. Sun, Y. Guo and H. He, A review on syntheses, properties, characterization and bioanalytical applications of fluorescent carbon dots, *Microchim. Acta*, 2016, **183**, 519–542.
34 X. Quin, C. Fu, J. Zhang, W. Shao, X. Quin, Y. Gui, L. Wang, H. Guo, F. Chen, L. Jiang, G. Wu, F. J. Bikker and D. Luo, Direct preparation of solid carbon dots by pyrolysis of collagen waste and their applications in fluorescent sensing and imaging, *Front. Chem.*, 2022, **10**, 1006389.
35 T. H. Chen and W. L. Tseng, Self-assembly of monodisperse carbon dots into high-brightness nanoaggregates for cellular uptake imaging and iron(III) sensing, *Anal. Chem.*, 2017, **89**, 11348–11356.
36 A. Pramanik, S. Biswas and P. Kumbhakar, Solvatochromism in highly luminescent environmental friendly carbon quantum dots for sensing applications: Conversion of bio-waste into bio-asset, *Spectrochim. Acta, Part A Mol. Biomol. Spectrosc.*, 2018, **191**, 498–512.
37 Hc Tan, Wh Zhao, Q. Qiu, R. Zhang, Yy Zuo and Lj Yang, Green synthesis of nitrogen-doped fluorescent carbon quantum dots for selective detection of iron, *Fullerenes, Nanotubes Carbon Nanostruct.*, 2017, **25**, 417–422.
38 P. Song, L. Zhang, H. Long, M. Meng, T. Liu, Y. Yin and R. Xi, A multianalyte fluorescent carbon dots sensing system constructed based on specific recognition of Fe(III) ions, *RSC Adv.*, 2017, **7**, 28637–28646.
39 A. McEnroe, E. Brunt, N. Mosleh, J. Yu, R. Hailstone and X. Sun, Bright, green fluorescent carbon dots for sensitive and selective detection of ferrous ions, *Talanta Open*, 2023, **7**, 100236.
40 Q. Ye, F. Yan, Y. Luo, Y. Wang, X. Zhou and L. Chen, Formation of N, S-codoped fluorescent carbon dots from biomass and their application for the selective detection of mercury and iron ion, *Spectrochim. Acta, Part A Mol. Biomol. Spectrosc.*, 2017, **173**, 854–862.
41 L. Ge, H. Yu, H. Ren, B. Shi, Q. Guo, W. Gao, Z. Li and J. Li, Photoluminescence of carbon dots and their applications in Hela cell imaging and Fe^{3+} ion detection, *J. Mater. Sci.*, 2017, **52**, 9979–9989.
42 T. Chatzimitakos, A. Kasouni, L. Sygellou, A. Avgeropoulos, A. Troganis and C. Stalikas, Two of a kind but different: Luminescent carbon quantum dots from citrus peels for iron and tartrazine sensing and cell imaging, *Talanta*, 2017, **175**, 305–312.
43 S. Wu, L. Fang, Y. Li, H. B. Wang and H. Zhang, A fluorescence turn on–off−on method for sensitive detection of Sn2+ and glycine using waste eggshell membrane derived carbon nanodots as probe, *J. Fluoresc.*, 2023, **33**, 1505–1513.
44 P. Gao, Z. Xie and M. Zheng, Chiral carbon dots-based nanosensors for Sn(II) detection and lysine enantiomers recognition, *Sens. Actuators, B*, 2020, **319**, 128265.
45 V. Sharma, A. K. Saini and S. M. Mobin, Multicolour fluorescent carbon nanoparticle probes for live cell

imaging and dual palladium and mercury sensors, *J. Mater. Chem. B*, 2016, **4**, 2466–2476.

46 W. Gao, H. Song, X. Wang, X. Liu, X. Pang, Y. Zhou, B. Gao and X. Peng, Carbon dots with red emission for sensing of Pt2+, Au3+, and Pd2+ and their bioapplications in vitro and in vivo, *ACS Appl. Mater. Interfaces*, 2018, **10**, 1147–1154.

47 M. Shamsipur, A. Barati, A. A. Taherpour and M. Jamshidi, Resolving the multiple emission centers in carbon dots: from fluorophore molecular states to aromatic domain states and carbon-core states, *J. Phys. Chem. Lett.*, 2018, **9**, 4189–4198.

48 X. W. Tan, A. N. B. Romainor, S. F. Chin and S. M. Ng, Carbon dots production via pyrolysis of sago waste as potential probe for metal ions sensing, *J. Anal. Appl. Pyrolysis*, 2014, **105**, 157–165.

49 Y. Li, J. Bi, S. Liu, H. Wang, C. Yu, D. Li, B. W. Zhu and M. Tan, Presence and formation of fluorescence carbon dots in a grilled hamburger, *Food Funct.*, 2017, **8**, 2558–2565.

50 P. Davis, *Flora of Turkey and the East Aegean Islands*, Vol. 1, UniversityPress, Edinburgh 1967.

51 POWO, Arenaria serpyllifolia L. | Plants of the World Online | Kew Science, 2025, https://powo.science.kew.org/taxon/urn:lsid:ipni.org:names:263221-1.

52 A. Gümrükçüoğlu, M. Ocak, S. Kolaylı, S. Dinç, I. Altin, S. Gün and Ü. Turgut Ocak, Spectrofluorometric determination of Fe^{3+}, Pd^{2+}, and Sn^{2+} ions using carbon nanodots derived from hazelnut shells, *Methods Appl. Fluoresc.*, 2025, **13**, 035002, DOI: 10.1088/2050-6120/add1aa.

53 I. F. Benzie and Y. T. Szeto, Total antioxidant capacity of teas by the ferric reducing/antioxidant power assay, *J. Agric. Food Chem.*, 1999, **47**(2), 633–636.

54 A. Pramanik, S. Biswas and P. Kumbhakar, Solvatochromism in highly luminescent environmental friendly carbon quantum dots for sensing applications: conversion of bio-waste into bio-asset Spectrochim, *Spectrochim. Acta, Part A*, 2018, **191**, 498–512.

55 R. Apak, K. Güçlü, M. Ozyürek and S. E. Karademir, Novel total antioxidant capacity index for dietary polyphenols and vitamins C and E, using their cupric ion reducing capability in the presence of neocuproine: CUPRAC method, *J. Agric. Food Chem.*, 2004, **52**(26), 7970–7981.

56 T. C. P. Dinis, V. M. C. Madeira and L. M. Almeida, Action of Phenolic Derivatives (Acetaminophen, Salicylate, and 5-Aminosalicylate) as Inhibitors of Membrane Lipid Peroxidation and as Peroxyl Radical Scavengers, *Arch. Biochem. Biophys.*, 1994, **315**, 161–169.

57 W. Gao, H. Song, X. Wang, X. Liu, X. Pang, Y. Zhou, B. Gao and X. Peng, Carbon dots with red emission for sensing of Pt2+, Au3+, and Pd2+ and their bioapplicationsin vitro and in vivo ACS, *ACS Appl. Mater. Interfaces*, 2018, **10**, 1147–1154.

58 F. Li, C. Liu, J. Yang, Z. Wang, W. Liu and F. Tian, Mg/N double doping strategy to fabricate extremely high luminescent carbon dots for bioimaging, *RSC Adv.*, 2014, **4**, 3201–3205.

59 M. Shamsipur, A. Barati, A. A. Taherpour and M. Jamshidi, Resolving the multiple emission centers in carbon dots: from fluorophore molecular states to aromatic domain states and carbon-core statesJ, *Phys. Chem. Lett.*, 2018, **9**, 4189–4198.

60 X. Ma, Y. Dong, H. Sun and N. Chen, Highly fluorescent carbon dots from peanut shells as potential probes for copper ion: the optimization and analysis of the synthetic process Mater, *Today Chem*, 2017, **5**, 1–10.

61 M. Liu, Optical Properties of Carbon Dots: A Review, *Nanoarchitectonics*, 2020, **1**(1), 1–12, DOI: 10.37256/nat.112020124.1-12.

62 Y. Liu, H. Huang, W. Cao, B. Mao, Y. Liu and Z. Kang, Advances in carbon dots: from the perspective of traditional quantum dots, *Mater. Chem. Front.*, 2020, **4**(6), 1586–1613, DOI: 10.1039/D0QM0.0090F.

63 W. Ma, B. Wang, Y. Yang and J. Li, Photoluminescent chiral carbon dots derived from glutamine, *Chin. Chem. Lett.*, 2021, **32**(12), 3916–3920, DOI: 10.1016/J.CCLET.2021.05.021.

64 S. Lai, Y. Jin, L. Shi, R. Zhou, Y. Zhou and D. An, Mechanisms behind excitation- and concentration-dependent multicolor photoluminescence in graphene quantum dots, *Nanoscale*, 2020, **12**(2), 591–601, DOI: 10.1039/c9nr08461d.

65 Y. P. Sun, B. Zhou, Y. Lin, W. Wang, K. A. S. Fernando, P. Pathak, M. J. Meziani, B. A. Harruff, X. Wang, H. Wang, P. G. Luo, H. Yang, M. E. Kose, B. Chen, L. M. Veca and S. Y. Xie, Quantum-Sized Carbon Dots for Bright and Colorful Photoluminescence, *J. Am. Chem. Soc.*, 2006, **128**, 7756–7757.

66 J. Zhang and S. H. Yu, Carbon dots: large-scale synthesis, sensing and bioimaging, *Mater. Today*, 2016, **19**, 382–393.

67 P. Babu, S. Mohanty, B. Naik and K. Parida, Serendipitous assembly of mixed phase BiVO4 on B−doped g−C3N4: An appropriate p−n heterojunction for photocatalytic O2 evolution and Cr(VI) reduction, *Inorg. Chem.*, 2019, **58**, 12480–12491.

68 Z.-Q. Zhao, L. Tan, T.-B. Lv, J.-J. Zhang, K.-M. Liao, H.-Y. Wang, Z. Zeng, S. Deng and G.-P. Dai, Carbon Quantum Dots with Room Temperature Phosphorescence for Information Encryption and Anticounterfeiting, *ACS Appl. Nano Mater.*, 2024, **7**(11), 13736–13744.

69 X. Jin, L. Tan, Z. Zhao, M. Li, Q. Zhou, J. Zhang and G. Dai, Facile synthesis of graphene quantum dots with red emission and high quantum yield, *New J. Chem.*, 2023, **47**, 2221–2229, DOI: 10.1039/D2NJ04491A.

70 Y. P. Sun, B. Zhou, Y. Lin, W. Wang, K. A. S. Fernando, P. Pathak, M. J. Meziani, B. A. Harruff, X. Wang, H. Wang, P. G. Luo, H. Yang, M. E. Kose, B. Chen, L. M. Veca and S. Y. Xie, Quantum-sized carbon dots for bright and colorful photoluminescence, *J. Am. Chem. Soc.*, 2006, **128**, 7756–7757.

71 M. Shamsipur, A. Barati, A. A. Taherpour and M. Jamshidi, Resolving the multiple emission centers in carbon dots: from fluorophore molecular states to aromatic domain states and carbon-core states, *J. Phys. Chem. Lett.*, 2018, **9**, 4189–4198.

72 Y. Çağlar, E. T. Saka, H. Alp, H. Kantekin, M. Ocak and Ü. Ocak, A simple spectrofluorimetric method based on quenching of a Nickel(II)-phthalocyanine complex to determine iron (III), *J. Fluoresc.*, 2016, **26**, 1381–1389.

73 T. Pal, S. Mohiyuddin and G. Packirisamy, Facile and green synthesis of multicolor fluorescence carbon dots from curcumin: In vitro and in vivo bioimaging and other applications, *ACS Omega*, 2018, **3**, 831–843.

74 J. Shen, S. Shang, X. Chen, D. Wang and Y. Cai, Highly fluorescent N, S-co-doped carbon dots and their potential applications as antioxidants and sensitive probes for Cr (VI) detection, *Sens. Actuators, B*, 2017, **248**, 92–100.

75 A. Sachdeva and P. Gopinath, Green synthesis of multifunctional carbon dots from coriander leaves and their potential application as antioxidants, sensors and bioimaging agents, *Analyst*, 2015, **140**, 4260–4269.

76 X. Zhang, H. Wang, C. Ma, N. Niu, Z. Chen, S. Liu, J. Li and S. Li, Seeking value from biomass materials: preparation of coffee bean shell-derived fluorescent carbon dots via molecular aggregation for antioxidation and bioimaging applications, *Mater. Chem. Front.*, 2018, **2**, 1269–1275.

77 L. A. A. Chunduri, A. Kurdekar, S. Patnaik, B. V. Dev, T. M. Rattan and V. Kamisetti, Carbon quantum dots from coconut husk: Evaluation for antioxidant and cytotoxic activity, *Mater. Focus*, 2016, **5**, 55–61.

78 H. Hamishehkar, B. Ghasemzadeh, A. Naseri and R. Salehi, Carbon dots preparation as a fluorescent sensing platform for highly efficient detection of Fe (III) ions in biological systems, *Spectrochim. Acta, Part A Mol. Biomol. Spectrosc.*, 2015, **150**, 934–939.

79 B. Shi, Y. Su, L. Zhang, M. Huang, R. Liu and S. Zhao, Nitrogen and phosphorus co-doped carbon nanodots as a novel fluorescent probe for highly sensitive detection of Fe^{3+} in human serum and living cells, *ACS Appl. Mater. Interfaces*, 2016, **8**, 10717–10725.

80 V. Singh and A. K. Mishra, Green and cost-effective fluorescent carbon nanoparticles for the selective and sensitive detection of iron (III) ions in aqueous solution: Mechanistic insights and cell line imaging studies, *Sens. Actuators, B*, 2016, **227**, 467–474.

81 X. Zhang, J. Lu, X. Zhou, C. Guo and C. Wang, Rapid microwave synthesis of N-doped carbon nanodots with high fluorescence brightness for cell imaging and sensitive detection of iron, *Opt. Mater.*, 2017, **64**, 1–8.

82 R. Vikneswaran, S. Ramesh and R. Yahya, Green synthesized carbon nanodots as a fluorescent probe for selective and sensitive detection of iron (III) ions, *Mater. Lett.*, 2014, **136**, 179–182.